PAPER • OPEN ACCESS

Role of pH in the synthesis and growth of gold nanoparticles using L-asparagine: a combined experimental and simulation study

IOP ebooks™

Bringing together innovative digital publishing with leading authors from the global scientific community.

Start exploring the collection–download the first chapter of every title for free.

Role of pH in the synthesis and growth of gold nanoparticles using L-asparagine: a combined experimental and simulation study

Ricardo Báez-Cruz[1,2] , **Luis A Baptista**[1] , **Samuel Ntim**[3] ,
Paulraj Manidurai[2], **Shirly Espinoza**[4] , **Charusheela Ramanan**[1] ,
Robinson Cortes-Huerto[1,*] and **Marialore Sulpizi**[3,*]

[1] Max Planck Institute for Polymer Research, Ackermannweg 10, 55128 Mainz, Germany
[2] Department of Physics, Faculty of Physical and Mathematical Science, University of Concepcion, PO Box 160-C, Concepcion, Chile
[3] Institut für Physik, Johannes Gutenberg Universität, Staudingerweg 7, 55128-Mainz, Germany
[4] ELI Beamlines, Institute of Physics, Czech Academy of Science, Za Radnici 835, 25241 Dolni Brezany, Czech Republic

E-mail: corteshu@mpip-mainz.mpg.de and sulpizi@uni-mainz.de

CrossMark

Abstract

The use of biomolecules as capping and reducing agents in the synthesis of metallic nanoparticles constitutes a promising framework to achieve desired functional properties with minimal toxicity. The system's complexity and the large number of variables involved represent a challenge for theoretical and experimental investigations aiming at devising precise synthesis protocols. In this work, we use L-asparagine (Asn), an amino acid building block of large biomolecular systems, to synthesise gold nanoparticles (AuNPs) in aqueous solution at controlled pH. The use of Asn offers a primary system that allows us to understand the role of biomolecules in synthesising metallic nanoparticles. Our results indicate that AuNPs synthesised in acidic (pH 6) and basic (pH 9) environments exhibit somewhat different morphologies. We investigate these AuNPs via Raman scattering experiments and classical molecular dynamics simulations of zwitterionic and anionic Asn states adsorbing on (111)-, (100)-, (110)-, and (311)-oriented gold surfaces. A combined analysis suggests that the underlying mechanism controlling AuNPs geometry correlates with amine's preferential adsorption over ammonium groups, enhanced upon increasing pH. Our simulations reveal that Asn (both zwitterionic and anionic) adsorption on gold (111) is essentially different from adsorption on more open surfaces. Water molecules strongly interact with the gold face-centred-cubic lattice and create traps, on the more open surfaces, that prevent the Asn from diffusing. These results indicate that pH is a relevant parameter in green-synthesis protocols with the capability to control the nanoparticle's geometry, and pave the way to computational studies exploring the effect of water monolayers on the adsorption of small molecules on wet gold surfaces.

(Some figures may appear in colour only in the online journal)

1. Introduction

Gold nanoparticle (AuNP) systems exhibit high biocompatibility and unique optical and catalytic properties, making them attractive for next-generation medical and imaging applications [1, 2]. Incorporating AuNPs into technology depends on successful size- and shape-engineering [3]. Previously, shape-control and synthesis of anisotropic particles has been achieved by the addition of surfactant agents such as hexadecyl(trimethyl)ammonium bromide (CTAB) [4]. However, these materials result in AuNPs with higher toxicity due to CTAB and contaminant by-products, limiting the widespread use of these AuNPs [5]. There is therefore significant interest in developing alternative, less toxic synthetic routes to shape-controlled AuNPs [6].

Protein- [7] and amino acid-based [8] synthesis protocols have been implemented to control the shape and size of the resulting nanoparticles. The group of 20 proteinogenic α-amino acids found in eukaryotes have been used to synthesise AuNPs, acting as both reducing and capping agents [9, 10]. These results indicate that the type of amino acid and experimental conditions determine the AuNPs quality. For example, changes in histidine concentration and pH enables adequate control of the size and particle shape [9]. By contrast, synthesis with L-asparagine (Asn) produces monodisperse AuNPs, and Asn concentration variation do not induce changes in the AuNPs color, size, or shape [11]. Alternatively, the pH of the amino acid solution is essential to control the reducing and functionalisation capabilities in AuNPs [12, 13]. This fact prompts the question as to whether pH can be used as an adjustable parameter to control AuNPs geometry.

In addition to experimental characterisation techniques such as transmission electron microscopy (TEM) [14], high-resolution transmission electron microscopy (HR-TEM) [15], ultraviolet–visible spectroscopy [16], and Raman spectroscopy [17], computational studies of AuNPs in chemical environments have been performed to resolve the intricate interaction mechanisms occurring at the metal–environment interface. These studies include *ab initio* density functional theory [18–20] and classical molecular dynamics (MD) simulations [21–26]. The typical AuNPs size (ranging from 2 to 10 nm), and the presence of solvent and surfactants, prevent the simulation of systems of realistic size. In this context, the study of simplified models of these systems provides valuable information on the metal surface, usually hidden by the surfactant. Moreover, it helps to predict equilibrium structures based on simple energetic arguments [19, 24, 25].

Here, we rely on a combined simulation-experimental approach to investigate the role of acidic (pH 6) and basic (pH 9) pH conditions in the AuNPs synthesis using Asn as both capping and reducing agent. This choice is motivated by the fact that the acidic (basic) environment is the result of a high concentration of the zwitterionic (anionic) Asn state. We expect that the two distinct chemical forms exhibit different interactions with gold surfaces thus impacting the AuNPs obtained at these pH conditions. In our experiments, we adjust the pH adding small volumes of a stock solution of 100 mM sodium hydroxide. The explicitly treatment of pH in MD simulations, however, is not obvious and is the subject of intense investigations [27]. Here, we do not attempt to adjust the pH of the environment/solution in the simulations explicitly. Instead, we consider zwitterionic and anionic states of Asn, whose excess in solution is related to acidic and basic pH conditions, respectively. We thus compare the adsorption of both Asn states on (111), (100), (110) and (311) gold surfaces, prevalent in the obtained AuNPs, focusing on the details of the interaction at the interface. Our MD simulations reveal that the adsorption of zwitterionic Asn on gold surfaces results from a competing effect between the attraction to the amide group, in agreement with *ab initio* simulations [18], and the slight repulsion of the ammonium group. By contrast, in the anionic state, the ammonium group is replaced by an amine group, and therefore Asn displays higher gold affinity. Raman spectra for Asn on gold at pH 6 and pH 9 confirm this picture with the respective rise of $-NH_3^+$ and decrease of $-NH_2$ intensities for these groups at their characteristic frequencies.

Our MD simulations also provide qualitatively different pictures for the adsorption on the considered gold orientations (crystalline planes). Asn lies essentially flat on (111) and is free to diffuse, with adsorption dominated by the amide group. For the remaining surfaces, the water molecules display a significant structuring, consistent with the underlying fcc structure, close to the gold surface (between 3 and 6 Å). This structure creates energetically favourable locations for Asn on open gold surfaces that prevent it from diffusing.

The paper is organised as follows: in section 2 we describe the synthesis procedure, characterisation techniques and the computational approach. We present and discuss our experimental and theoretical results in section 3. Finally, we conclude in section 4.

2. Materials and methods

All chemicals were of analytical grade and were used without further purification. Gold(III) chloride acid trihydrate
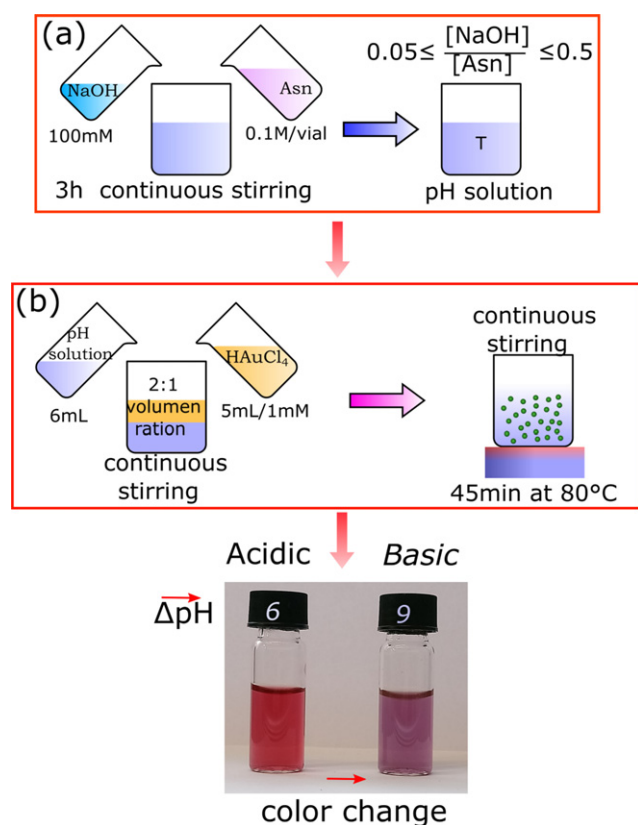
Figure 1. Schematic representation of AuNPs synthesised by Asn as a reducing agent. (a) In the first synthesis part, the Asn is first dissolved in water, and the Asn pH is controlled by a molar ratio of NaOH vs Asn. (b) In the second synthesis part, Asn solutions are then mixed with HAuCl₄ in varying ratios. The photograph indicates the color difference between AuNP products synthesised at different pH. The acidic solution at pH 6 appears red to the eye while the more basic solution at pH 9 appears purple.
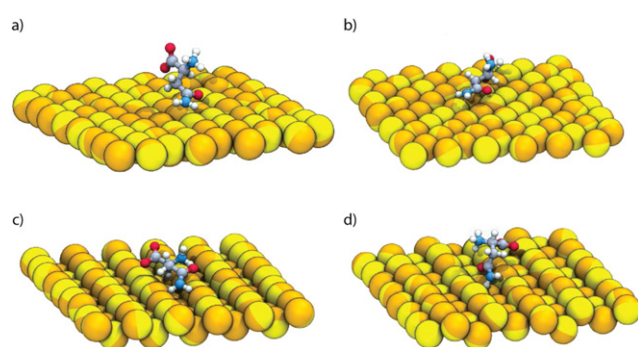

Figure 2. Simulation snapshots showing Asn on (a) (100), (b) (111), (c) (110), and (d) (311) gold surfaces. For the sake of clarity, water molecules are not shown.

(HAuCl₄ · 3H₂O) (99.9%) and Asn (L-asparagine) (98.0%) were purchased from Sigma-Aldrich. Sodium hydroxide (NaOH, pastilles, from Molar) was used to adjust the pH. The water used in all experiments was prepared using a Milli-Q Integral water purification system (EMD Millipore Direct -Q® 3UV-R) and had a resistivity of 18.2 MΩ cm.
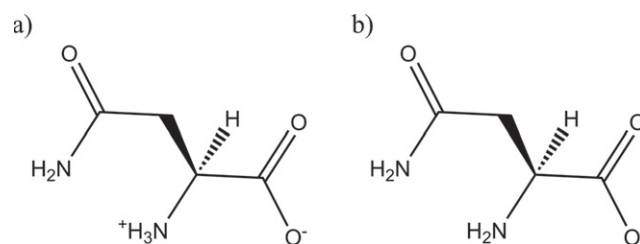

Figure 3. Schematic representation of Asn in the zwitterionic (major species at pH 6) (a) and anionic (major species at pH 9) (b) states.

2.1. Sample preparation

100 ml of 100 mm Asn solution was prepared and separated into two vials of 6 ml solution. Different ratios R = [NaOH]/[Asn] of 0.05 and 0.5, with an interval step of 0.05 were created to obtain a pH variation on each sample. The NaOH/Asn mixtures (pH-adjusted Asn solution) were left, in closed vials, under constant stirring for 3 h at room temperature and under ambient conditions to reach pH equilibrium, as shown figure 1. Then, 6 ml of the pH-adjusted Asn solution was added to 5 ml of a 1 mm fresh Gold(III) chloride acid trihydrate (HAuCl₄ · 3H₂O) solution at room temperature. The mixtures were immediately mixed and incubated at 80 °C for 40 min using a hotplate. The samples were left to cool down at room temperature and without external cooling source. Subsequently, the set of samples were centrifuged at 1000 rpm, and the supernatant was extracted as the final product. Finally, we chose two pH, one more acid (pH 6) and one more basic (pH 9), for our studies.

2.2. Characterisation

Particle size, morphologies, and interplanar spacing in AuNPs were studied using a transmission electron microscope (TEM, JEOL JEM-2010) and high-resolution (HR)-TEM (Tecnai F20 microscope with FEI, acceleration voltage 200 kV) respectively. Gatan Digital Micrograph software was used to analyse the HR-TEM micrographs. Particle distribution and population were determined by ImageJ software with standard plug-ins, included for ∼100 particles per sample. The polydispersity (*P*) was estimated as

$$P = \frac{\sigma}{s}100\%, \tag{1}$$

with σ the standard deviation, σ = FWHM/2, FWHM the full width at half maximum of the total distribution, and *s* is the mean particle diameter (in nm).

The crystallographic toolbox (CrysTBox) software was used to interpret diffraction patterns obtained from HR-TEM micrographs [28]. The vibrational mode of Asn was characterised by Raman scattering. Raman spectra were acquired on a modular multi-channel Raman spectrograph Jobin Yvon–Spex 270M in 90° scattering geometry using a 532.15 nm line of a continuous-wave solid-state Nd-YAG laser for excitation, as described in references [29, 30]. The power at the sample was 240 mW [supplementary figure 3 in the SI (https://stacks.iop.org/CM/33/254005/mmedia)].Raman
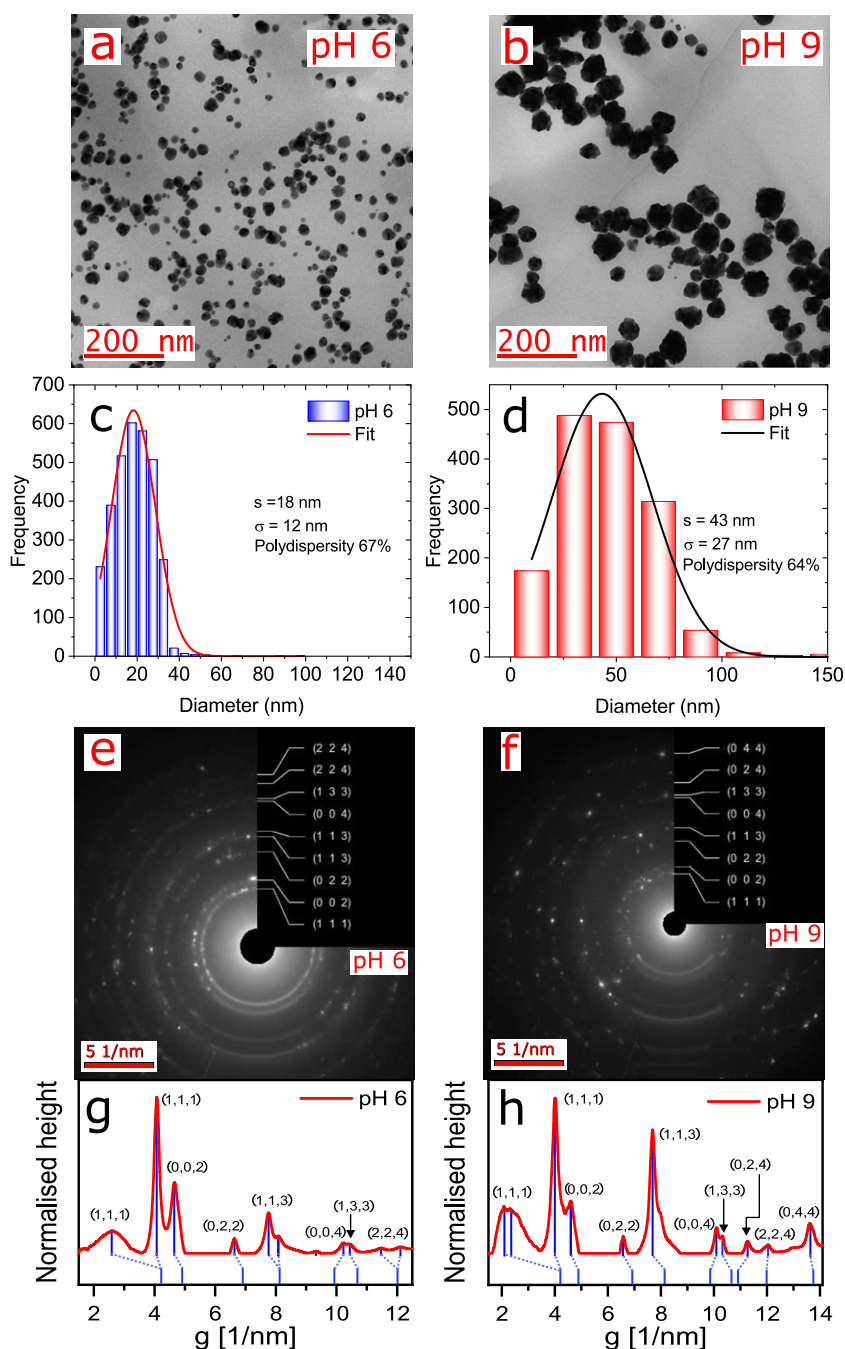
Figure 4. Morphological characterisation with electron microscopy shows different size and shape distributions emerge when AuNPs are synthesised with Asn at pH 6 vs pH 9. (a) Electron microscopy image at 200 nm of AuNPs at pH 6. (b) Electron microscopy image 200 nm of AuNPs at pH 9. (c) Histogram of the AuNP size distribution at pH 6 with a frequency over 600 counts. (d) Histogram of the AuNP size distribution at pH 9 with a frequency over 550 counts. (e) Electron diffraction pattern of AuNPs at pH 6. (f) Electron diffraction pattern of AuNPs at pH 9. (g) Electron diffraction profile of image (e) at pH 6. (h) Electron diffraction profile of image (f) at pH 9. In both cases, the electron diffraction pattern showed the (111), (200), (220), and (311) reflections of gold in a typical fcc structure.

measurements were performed at room temperature-controlled hermetical quartz cell (2 mm). Spectra were acquired with 5 s accumulation time, 12 accumulations and 15 spectra per sample. Wavenumber scales were precisely calibrated (± 0.1 cm^{-1}) using the emission spectra of a neon glow lamp taken before and after each Raman measurement. The Raman contribution from the water was subtracted, and the spectra were corrected for the non-Raman background.

2.3. Simulations

We investigate the adsorption of Asn on (111), (100), (110) and (311) gold surfaces (figure 2) by first calculating the potential of mean force (PMF) resulting from pulling the amino acid away from the surface and towards the bulk water. Gold surfaces are oriented with normal vector parallel to the z-axis. Initially, we place the Asn as close as possible to the gold surface, at a distance of ~ 0.3 nm. The simulation boxes were
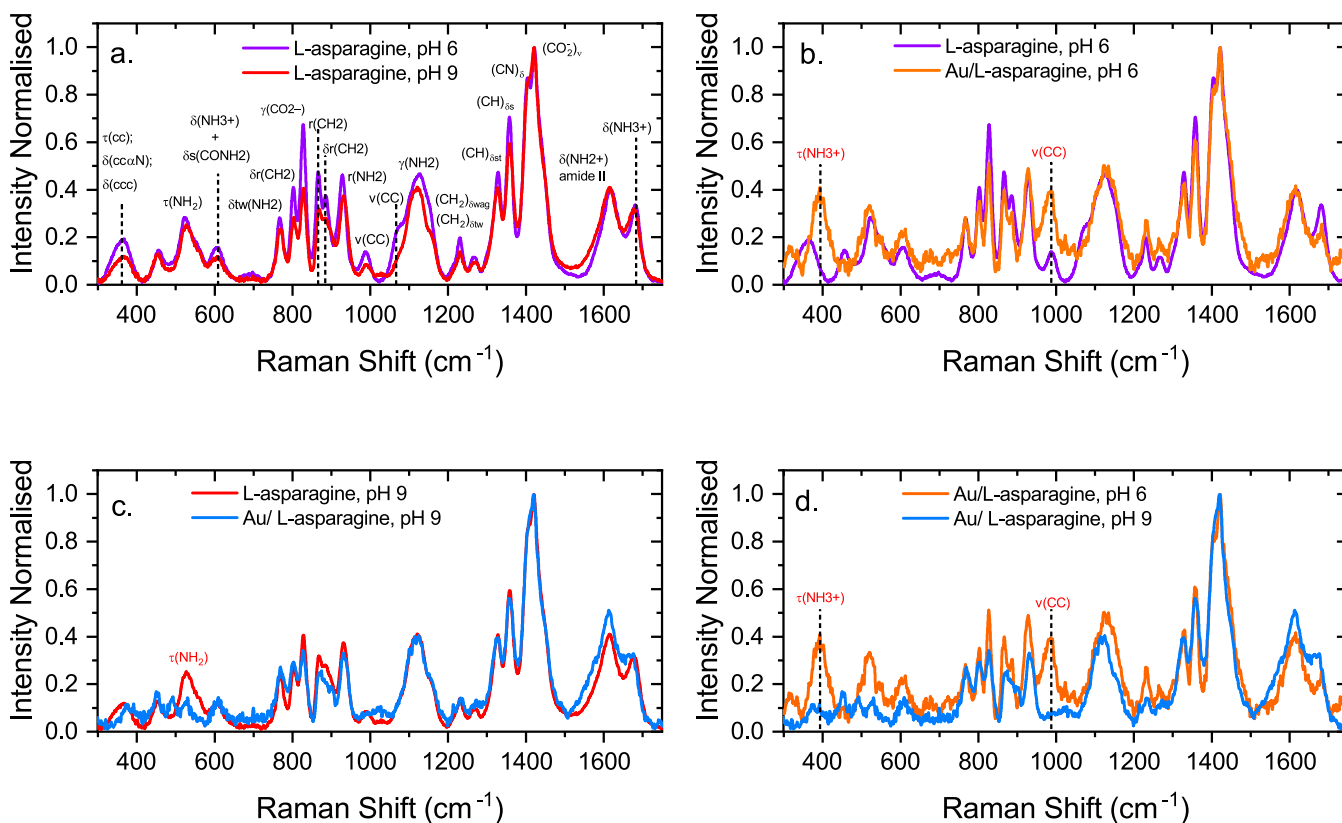
Figure 5. Experimental Raman spectra at pH 6 and 9 for the samples of AuNPs/Asn. (a) Raman spectra of Asn at pH 6 and 9. (b) Raman spectra of Asn at pH 6AuNPs/Asn at pH 6. (c) Raman spectra of Asn at pH 9 and AuNPs/Asn at pH 9. (d) Raman spectra of AuNPs/Asn at pH 6 and pH 9.

filled with TIP3P water molecules [31]. The centre of mass (COM) of Asn molecule was pulled out in the *z* direction and snapshots were collected each 0.1 nm in order to generate the starting configurations for the umbrella sampling calculation. For each window, 9 ns of MD simulation were performed with the Asn COM constrained using a harmonic potential with spring constant of 1000 kJ mol^{-1} nm^{-2}.

The PMF for each system was reconstructed using the weighted histogram analysis method [32]. All simulations were carried out with GROMACS 5.1.2 [33, 34], using CHARMM general force field for organic molecules [35, 36], for both Asn states, and a polarisable force field for gold [37].

In the experiment, different values of pH are associated to an excess in the concentration of zwitterionic (acidic, pH 6) or anionic (basic, pH 9) states of Asn. We use a major approximation to mimic these pH conditions by studying the adsorption of a single Asn molecule in two states: zwitterionic and anionic (figure 3). To evaluate the adequacy of our approximation, we perform density functional theory simulations for a single Asn molecule in the two charge states and compute their corresponding Raman spectra (supplementary figure 6(a) in the SI). As expected, the spectrum of the anionic state exhibits suppressed resonances related to vibrations of the $-NH_3^+$ group. To a lesser degree, this effect is also apparent in the experimental Raman spectra of Asn in bulk solution at both pH conditions (figure 5(a)). This correspondence suggests that the simplification of identifying molecular states with pH conditions might

be useful to approximate and investigate the complex experimental conditions, which are inaccessible to computer simulations that explicitly include all the chemical species present in the system.

3. Results and discussion

3.1. Experiments

3.1.1. Morphological characterisation. TEM images (figure 4) show AuNPs (at 200 nm resolution) obtained by reacting gold(III) (HAuCl$_4$ · 3H$_2$O) with Asn at acidic (pH 6, figure 4(a)) and basic (pH 9, figure 4(b)) conditions. These images show that both reaction conditions yield non-spherical particles with increasingly amorphous shapes apparent at pH 9 (see also figures 3 and 4 in the SI). The average particle size was determined by analyzing twenty TEM micrographs and a minimum of 56 particles per sample (supplementary figures 1 and 2 show a gallery of TEM micrographs used in the calculation of the particle size distribution), and using standard imaging protocols with the ImageJ software package. The results from the particle size analysis are given in the histograms depicted in figure 4(c) (pH 6) and figure 4(d) (pH 9). A Gaussian fit to the size distribution shows that the pH 6 reaction conditions yield particles of 18 ± 12 nm diameter, while the pH 9 reaction condition resulted in larger particles of 43 ± 27 nm diameter. The polydispersities for each sample

Table 1. Frequency modes of Asn and assignments in the region of 300–1750 cm^{-1}. Abbreviations indicate: s = strong, m = medium, w = weak, v = very, sh = shoulder, sc = scissoring, r = rocking, wag = wagging, tw = twisting, ν = stretching, δ = bending, γ = out-of-plane bending, τ = torsion, s = symmetric, a = antisymmetric.

Frequency (cm^{-1})	Assignments	Reference
364	δ(CCC); δ(CC$^\alpha$ N); τ(CC)	[39]
400	τ(NH$_3^+$)	[40]
455		
522	τ(NH$_2$)	[41]
608	δ(NH$_3^+$) + δ_s(CONH$_2$)	[39]
700		
776		
802	δ_r(CH$_2$)/δ_{tw}(NH$_2$)	[42–44]
825	γ(CO$_2^-$)	[39]
836	γ(NH$_2$)	[41]
865	r(CH$_2$)	[40]
884	δ_r(CH$_2$)	[43]
928	r(NH$_2$)	[44]
987	ν(CC)	[42]
1077	ν(CN)	[39]
1125	γ(NH$_2$)	[39]
1231	δ_{tw}(CH$_2$)/δ_{wag}(CH$_2$)	[40]
1266	w(CH$_2$)	[40]
1329	δ(CH)	[44]
1357	δ(CH) δ_s(CH)	[42]
1404	δ(CN) AIII	[44]
1420	δ_s(CO$_2^-$)/δ_{sc}(CH$_2$)	[40]
1617	δ(NH$_2^+$) amide II	[42]
1680	δ(NH$_3^+$)	[44]
2129		
2940	νu_s(CH$_2$)	[41]
3195		
3233	Water	[39]
3428	Water	[39]

set were similar, calculated as 67% for pH 6 and 64% for pH 9. These results indicate that, on average, the pH 6 particles are approximately 25 nm smaller in diameter than the pH 9 particles.

The electron diffraction pattern from the TEM measurements are shown in figures 4(e) and (f), and the corresponding electron diffraction profiles of figures 4(e) and (f) are shown in figures 4(g) and (h) for pH 6 and 9 respectively. The primary diffraction peaks correspond to (111), (200), (220), and (311) reflections, which are characteristic of the gold fcc structure [38]. The relative intensities of the diffraction peaks vary between the two sample sets, suggesting a difference in the particle shape.

The surface structure of the particles were further analyzed using high-resolution TEM (supplementary figures 3 and 4). For the pH 6 samples, two well-resolved (222)-type crystallographic planes were detected (measured D-spacing of about 1.16 Å and 1.14 Å, as shown in supplementary figure 3(c)), which run perpendicular to the sidewalls of the structure. The same process was used in the sample at pH 9, but in this case, was not apparent to identify crystalline orientations on the

particle surface. Only one vertex selected shows (111)-type crystallographic planes (measured D-spacing of about 2.35 Å, as shown in supplementary figure 4(c)), which like the previous case run perpendicular to the sidewalls of the structure. The high-resolution TEM images at 10 nm showed differences in particle surface geometry between the two cases (supplementary figures 3(b) and 4(b)). In the case of pH 6, it was possible to identify four triangular partitions on the particle surface with angles of 114.5°, 87.3°, 63.1°, and 28.2° (supplementary figure 3(b)). In comparison, with the particles at pH 9, it was not possible to identify partitions on the particle surface. The pH 9 sample could not be similarly fit further indicating highly homogeneous surface structure.

The morphological characterisation indicates that the pH 6 samples are on average smaller and more homogeneous in surface geometry than the pH 9 samples.

Earlier work in the literature has shown that when Asn is used as a reducing agent to produce AuNPs, the size, color, and shape do not depend on the reactant concentrations [11]. Our results here demonstrate that when the reaction pH is used as a tuning parameter, it is possible to modify the critical properties of size, color, and shape.

3.1.2. Vibrational spectroscopic characterisation. Figure 5 shows the measured Raman spectra of the AuNPs, along with two solutions of Asn in water, at pH 6 and 9, for reference. Figure 5(a) shows the normalised Raman spectra of the reference solutions in the frequency region of 300 cm^{-1} to 1750 cm^{-1}, along with mode assignments. The mode ν(CO$_2^-$) shows the highest intensity for both solutions. In the frequency region of 700 cm^{-1} to 1000 cm^{-1}, the Asn solution at pH 9 shows a decrease in the intensity of the modes compared to the Asn solution at pH 6 (figure 5(a)). Relevant shifts of the peaks in the spectra were not detected. Figure 5(b) shows a comparison of the normalised Raman spectra for the Asn solution in water at pH 6 and the AuNPs/Asn sample at pH 6. The sample AuNPs/Asn at pH 6 presents a peak at 400 cm^{-1}, which is associated to a torsion of –NH$_3^+$ group (τ(NH$_3^+$)). The mode τ(NH$_3^+$) was not detected on the solution of Asn in water. In the region of 987 cm^{-1} the stretching mode of ν(CC) underwent an increase in intensity compared to the spectrum of the solution of Asn in water. Figure 5(c) shows the comparison of the solution of Asn in water at pH 9 and the sample of AuNPs/Asn at pH 9. In this case, the spectrum of the AuNPs/Asn sample at pH 9 lacks the peak corresponding to the torsion mode of the –NH$_2$ group at 522 cm^{-1}. Figure 5(d) compares the Raman spectra of the samples AuNPs/Asn at pH 6 and AuNPs/Asn at pH 9. The main differences are the presence of the modes τ(NH$_3^+$) and ν(CC) in the sample AuNPs/Asn at pH 6 compared to the sample at pH 9, and a peak shift towards higher energies in the region of 1125 cm^{-1}, associated with out-of-plane bending mode of γ(NH$_2$) group for the sample with lower pH.

A summary of the assignment of the Raman peaks for Asn in the frequency region of 300 cm^{-1} to 1750 cm^{-1} is shown in table 1.
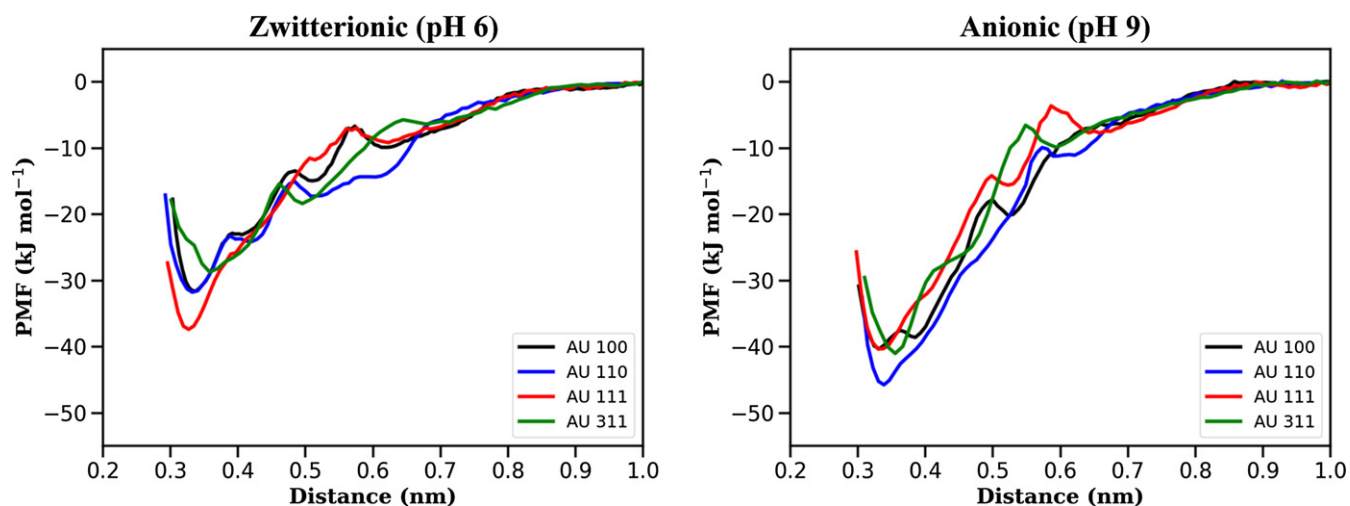
Figure 6. PMF obtained by pulling the COM of Asn in zwitterionic (left) and anionic (right) states from (100)-, (110)-, (111)- and (311)-oriented gold surfaces. We identify the zwitterionic and anionic states with pH 6 and pH 9, respectively.
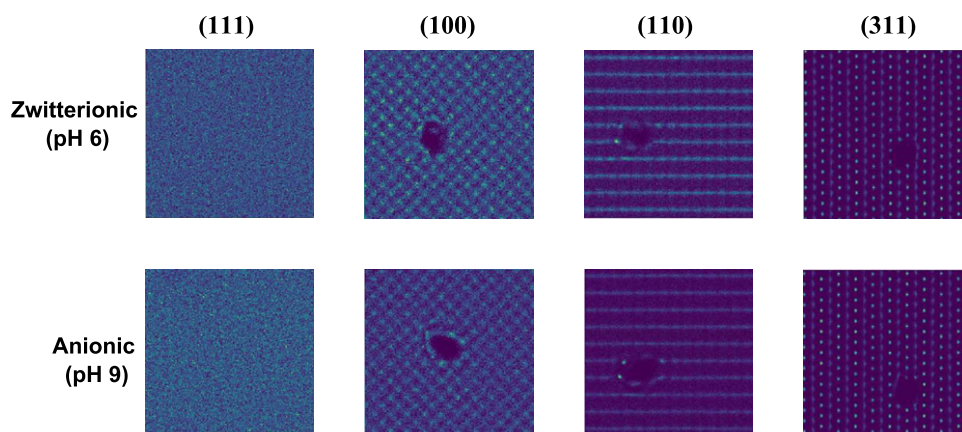

Figure 7. Projection, parallel to the surface, of the density of the oxygen atoms in water at a distance from the surface between 0.30 nm and 0.60 nm. In all cases, the Asn is in the equilibrium position corresponding to the given surface (between 0.3 nm and 0.4 nm).

3.2. Simulations

We investigate the adsorption mechanism of Asn on gold surfaces with orientations corresponding to the planes (111), (100), (110) and (311), which are those that most commonly appear in the experimental TEM spectra. We compute the PMF to quantify the affinity of the Asn with these surfaces. In figure 6 we present free energy profiles resulting from pulling Asn in the zwitterionic and anionic states which we associate to the two experimental conditions, namely pH 6 and pH 9, respectively. For all the considered surfaces, it is apparent that the anionic Asn tends to bind more strongly to the gold surfaces. It is also clear that close to the surface ($\sim$0.35 nm) the binding strength follows the trend (311) < (110) $\sim$ (100) < (111) for the zwitterionic Asn. For the anionic state, the trend changes to (111) $\sim$ (100) $\leqslant$ (311) < (110), where the PMF for (111) gains 2.9 kJ mol^{-1} upon increasing pH.

To shed light on the specifics of the adsorption process, we first focus on the minimum distance between the Asn COM and the surface. These distances are distributed between

0.3 nm and 0.4 nm. In figure 7 we show a projection of the density of the water oxygens, parallel to the surface, taken over a production run of 9 ns, and at a distance between 0.30 nm and 0.60 nm. The Asn COM is constrained along the *z*-direction and is free to move on the surface. From figure 7, the voids present for the two Asn states and the (100)-, (110)- and (311)-oriented surfaces indicate that the Asn remains pinned on the surface and it does not diffuse during the simulated timescale. By contrast, the amino acid freely diffuses on the (111)-oriented surface. As presented in figure 8, this effect is the result of the water ordering occurring in close proximity to the gold surface, in close registry with the fcc lattice. For the (111) case, this ordering is only observed for the first water layer (at $\sim$0.3 nm). For the remaining surfaces, the effect is apparent up to distances between 0.6 nm and 0.9 nm. Given the polar character of the Asn, it is not surprising that it forms a rather stable hydrogen network with water molecules close to the gold surface. Furthermore, for (100), (110) and (311) surfaces where the water structuring grows into the bulk, the hydrogen network creates a pocket for the amino acid that
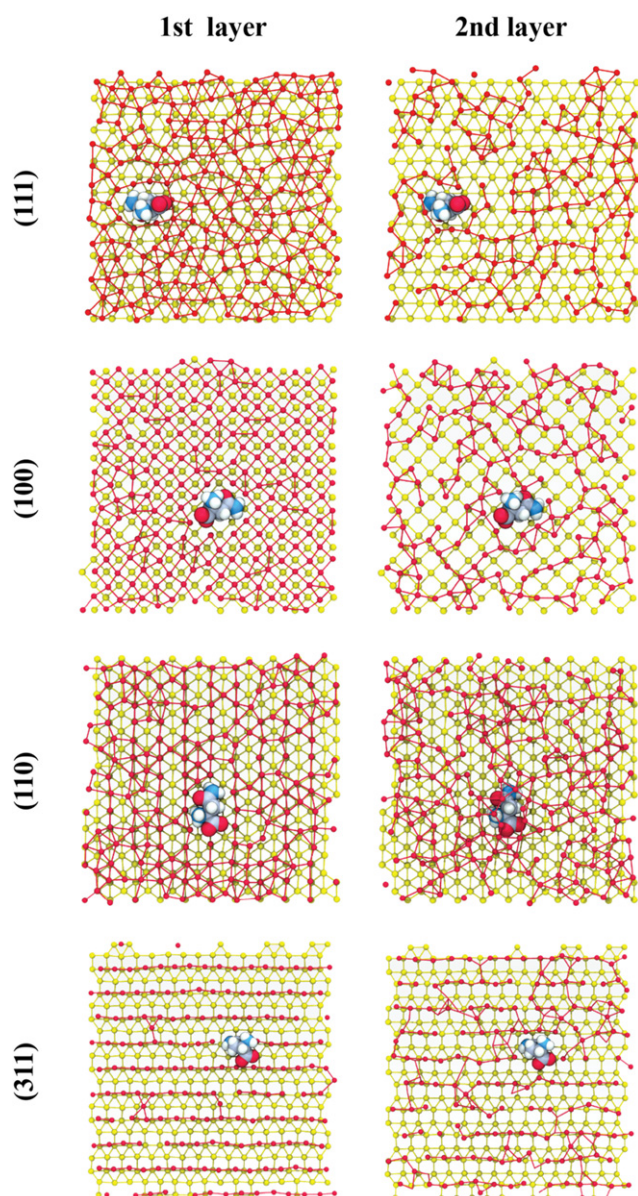
1st layer   **2nd layer**

(111)

(100)

(110)

(311)

Figure 8. Simulation snapshot showing the top view of first and second layers of water oxygen and the zwitterionic Asn on (a) (111), (b) (100), (c) (110), and (d) (311) gold surfaces. Key: water oxygen atoms in red, gold atoms in yellow. Bonds were designated with a cutoff of 3.7 Å.

hinders its surface diffusion. This picture remains essentially the same for the two Asn states considered here.

The rather uniform (111) surface facilitates the adsorption of Asn as can be seen in the PMF results. The amino acid lies essentially flat thus maximising its contact area with the surface. Upon pulling away the amino acid, we observe that the resulting PMF is somewhat barrierless, indicating that Asn is uniformly detaching from the (111) surface. For the other surfaces, the various minima in the PMF are associated to tilting angles between the amino acid and the surface, formed during the detaching process.

When going from the zwitterionic to the anionic state, the $-NH_3^+$ group is replaced with a $-NH_2$ group. This change does not significantly modify the adsorption on the uniform (111)

surface, as evidenced by the PMF (figure 6). For the open surfaces, this change in the charge of the amino acid results in an increase in the amino acid/surface attraction due to the presence of two $-NH_2$ groups which bind more favourably to gold. Figure 9 shows the distribution of distances of the amide group (black line) and the ammonium/amine (blue line) for the surface orientations considered when the COM of the Asn is at ~ 0.4 nm from the surface. The wide distribution without a clear preferential binding between the two groups is apparent for the (111) case. For the remaining surface orientations at acidic pH, it is clear that the amide group has the tendency to stay closer to the surface. At basic pH, both amine and amide groups are equally spaced from the surface. The complex distributions observed for the (110) case are the result of the tendency for Asn to align with the rows present on the surface.

These observations allows the interpretation of the Raman spectra presented in figure 5. At pH 6, panel (b), we observe that a peak at approximately 400 cm^{-1} develops in the presence of AuNPs. This frequency corresponds to the $\tau(NH_3^+)$ mode. Upon adsorption, the amine group, $-NH_2$, binds to the surface while the ammonium group, $-NH_3^+$, is free to move and vibrates at its characteristic frequency, thus generating the peak in the spectra. At pH 9, panel (c), the amino acid is mostly present in its anionic form with the ammonium replaced by an amine group. As shown in the figure, the adsorption of these two $-NH_2$ groups on the gold surface suppress the corresponding $\tau(NH_2)$ mode at approximately 550 cm^{-1}.

The molecular orientation also provides a possible interpretation of the diffraction pattern and TEM measurements. The equilibrium shape of a metal NP corresponds to the minimum surface area configuration that minimises the surface Gibbs free energy. By combining extended Wulff construction [45] approaches with known values of surface energies, it is possible to determine the NP final equilibrium shape [46]. In the case of Au surfaces in vacuum, there is an approximately linear relation between surface energy, σ, and number of broken bonds per unit area [24]

$$\sigma \approx \gamma \frac{\sum_i^{N_s} n_i}{S}, \qquad (2)$$

where γ is a constant in units of energy-per-atom, N_s the number of undercoordinated atoms per unit cell, n_i the number of Au broken bonds and S the area of the unit cell. *Ab initio* calculations predict that the product σS gives energies per atom equal to 55.6, 81.3 and 120.3 kJ mol^{-1} for (111), (100) and (110) Au surfaces, respectively [47]. Hence, the resulting AuNP equilibrium shape corresponds to a truncated octahedron exhibiting mostly (111) and (100) facets. The effect of including the interaction with a complex chemical environment is rationalised by considering a net overall decrease in Au surface energy and a deviation from the linear behaviour presented in equation (2) (with $\gamma \to 0$) [24]. This combined effect leads to the stabilisation of multi-faceted NPs [25].

The results in figure 6 indicate that the adsorption of a single Asn helps reducing the energetic cost necessary for surface stabilisation by an amount between 28.7 and 45.8 kJ mol^{-1} (see table 2). In the zwitterionic state (figure 6 left panel),
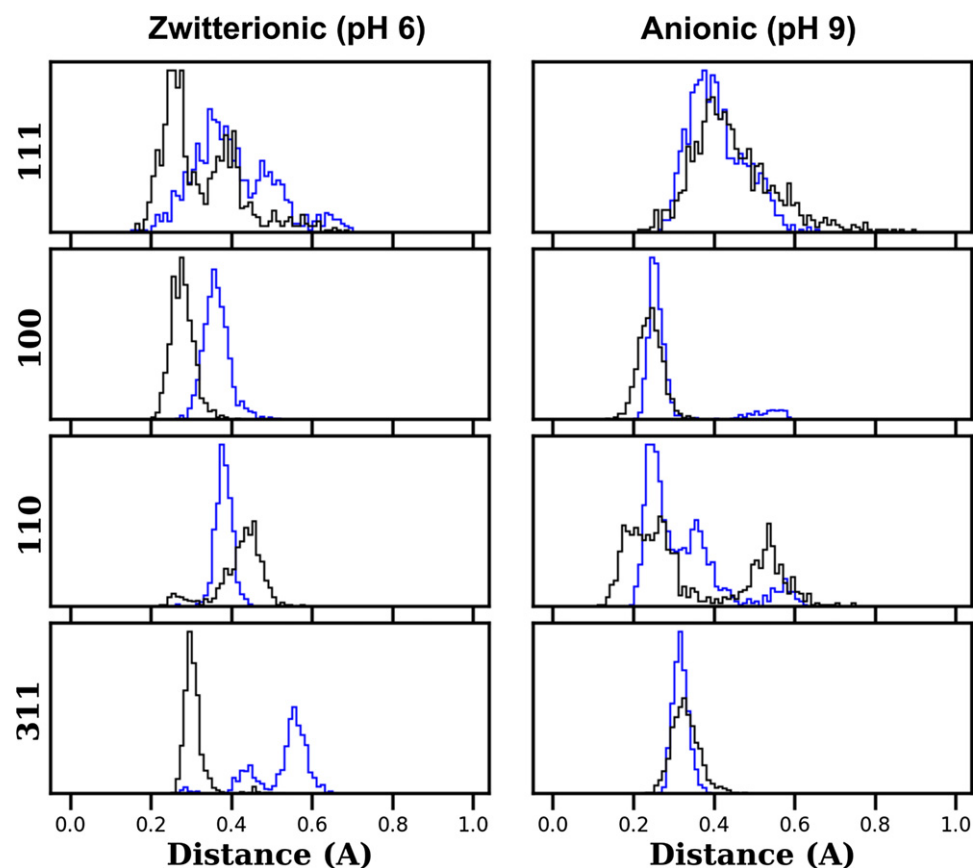
Figure 9. Distribution of distances of the ammonium/amine groups (blue lines) and amide group (black line) when the COM is constrained at ∼0.4 nm from the surface.

Table 2. Minimum energy values, and corresponding surface-Asn distances, of the PMF curves presented in figure 6.

Surface	Zwitterionic (pH 6)		Anionic (pH 9)	
	E (kJ mol^{-1})	d (nm)	E (kJ mol^{-1})	d (nm)
111	−37.4	0.327	−40.3	0.330
100	−31.6	0.338	−40.3	0.332
110	−31.8	0.332	−45.8	0.339
311	−28.7	0.358	−41.0	0.355

Asn interacts preferentially with the (111) surface with a free energy gain of 5.6 kJ mol^{-1} with respect to the (110) surface. This suggests that, upon Asn adsorption, the Au(111) facet is further stabilised with respect to the other facets, leading to rather isotropic AuNPs whose shape resembles the truncated octahedrons extensively discussed in the literature [48]. This prediction is consistent with HR-TEM and electron diffraction measurements shown in figures 4(e) and (f).

For the anionic state (figure 6 right panel), the main difference with the previous case is a general increase in Asn adsorption energy showing a reversal in the stabilisation sequence (see table 2). In this case the amino acid is more strongly bound to the (110) surface (5.5 kJ mol^{-1} with respect to (111)). In the context of equation (2), these conditions correspond to an overall stabilisation of Au surfaces, with an additional decrease

in surface energy differences between closed and open facets. As a result, open facets are more likely to appear, which agrees with scattering data showing higher population of (311) facets for basic than for acidic pH conditions (figures 4(g) and (h)). This could also qualitatively explain the HR-TEM micrographs at pH 9 showing relatively amorphous AuNPs (figures 2 and 4(b) in the SI). We emphasise here that the interaction with anionic Asn induces global stability and near degeneracy of Au surfaces leading to changes in morphology and size of the resulting NPs. Indeed, stabilisation of more open surfaces could also be the reason why we observe larger NPs at pH 9 (figure 4(d)). Stable open surfaces occupy larger surface areas that grow with the radius (square) of the NP.

4. Conclusions

The use of biomolecules to synthesise AuNPs combines functionality with maximum biocompatibility. The complexity of the system and the large number of experimental degrees of freedom requires the combination of simplified yet relevant computational models and controlled experimental conditions. With this aim, we use a single amino acid, Asn, to synthesise AuNPs in aqueous solution with controlled pH. We show that the resulting size, and to some extent the morphology of the AuNPs, depends on pH.

A combination of Raman scattering and MD simulations of the adsorption of zwitterionic and anionic Asn on (111)-, (100)-, (110)- and (311)-oriented gold surfaces unveils a unique adsorption mechanism. Asn mainly binds to gold surfaces via its amide group. Thus, the anionic state, the most probable state at higher pH (9 in the experiments), exhibits stronger binding to gold surfaces than the zwitterionic states, typical at acidic pH. In the latter, Asn preferentially adsorbs on (111) whereas, in the former, Asn preferentially adsorbs on the more open (110) and (311) surfaces. We use an argument based on surface energy considerations to suggest that this difference in Asn adsorption qualitatively explains why the AuNPs obtained at pH 9 are larger and somewhat amorphous when compared to the ones obtained at pH 6.

Our simulation results also highlight the role of water monolayers, close to the gold surface, in the adsorption of Asn. Water molecules on open gold surfaces order following the gold fcc template. The water structuring creates traps for Asn that prevent it from diffusing on the surface. The underlying mechanism deserves further examination; in particular, more simulations using amino acids with different water affinities would be beneficial to understand this caging effect.

Acknowledgments

Data availability statement

The data that support the findings of this study are available upon reasonable request from the authors.

ORCID iDs

Ricardo Báez-Cruz https://orcid.org/0000-0001-5315-5063
Luis A Baptista https://orcid.org/0000-0002-1419-6070
Samuel Ntim https://orcid.org/0000-0002-9549-0609
Shirly Espinoza https://orcid.org/0000-0002-2740-7156
Charusheela Ramanan https://orcid.org/0000-0001-8603-6853
Robinson Cortes-Huerto https://orcid.org/0000-0002-4318-970X
Marialore Sulpizi https://orcid.org/0000-0002-7810-3224

References

[1] Mahato K, Nagpal S, Shah M A, Srivastava A, Maurya P K, Roy S, Jaiswal A, Singh R and Chandra P 2019 Gold nanoparticle surface engineering strategies and their applications in biomedicine and diagnostics *3 Biotech* **9** 57
[2] Requejo K I, Liopo A V and Zubarev E R 2020 Gold nanorod synthesis with small thiolated molecules *Langmuir* **36** 3758–69
[3] Nehl C L and Hafner J H 2008 Shape-dependent plasmon resonances of gold nanoparticles *J. Mater. Chem.* **18** 2415–9
[4] Murphy C J, Sau T K, Gole A M, Orendorff C J, Gao J, Gou L, Hunyadi S E and Li T 2005 Anisotropic metal nanoparticles: synthesis, assembly, and optical applications *J. Phys. Chem.* B **109** 13857–70
[5] Lau I P, Chen H, Wang J, Ong H C, Leung K C-F, Ho H P and Kong S K 2012 *In vitro* effect of CTAB- and PEG-coated gold nanorods on the induction of eryptosis/erythroptosis in human erythrocytes *Nanotoxicology* **6** 847–56
[6] Si A, Pal K, Kralj S, El-Sayyad G S, de Souza F G and Narayanan T 2020 Sustainable preparation of gold nanoparticles via green chemistry approach for biogenic applications *Mater. Today Chem.* **17** 100327
[7] Chakraborty I, Feliu N, Roy S, Dawson K and Parak W J 2018 Protein-mediated shape control of silver nanoparticles *Bioconjugate Chem.* **29** 1261–5
[8] Courrol L C and de Matos R A 2016 Synthesis of gold nanoparticles using amino acids by light irradiation *Catalytic Application of Nano-Gold Catalysts* ed N K Mishra (London: IntechOpen) pp 83–99
[9] Maruyama T, Fujimoto Y and Maekawa T 2015 Synthesis of gold nanoparticles using various amino acids *J. Colloid Interface Sci.* **447** 254–7
[10] Hughes A B 2013 *Amino Acids, Peptides and Proteins in Organic Chemistry, Analysis and Function of Amino Acids and Peptides* vol 5 (New York: Wiley)
[11] Ghodake G, Vassiliadis V S, Choi J-H, Jang J and Lee D S 2015 Facile synthesis of gold nanoparticles by amino acid asparagine: selective sensing of arsenic *J. Nanosci. Nanotechnol.* **15** 7235–9
[12] Joshi H, Shirude P S, Bansal V, Ganesh K N and Sastry M 2004 Isothermal titration calorimetry studies on the binding of amino acids to gold nanoparticles *J. Phys. Chem.* B **108** 11535–40
[13] Csapó E, Ungor D, Kele Z, Baranyai P, Deák A, Juhász Á, Janovák L and Dékány I 2017 Influence of pH and aurate/amino acid ratios on the tuneable optical features of gold nanoparticles and nanoclusters *Colloids Surf.* A **532** 601–8

[14] Eric Hayat M A 2012 *Basic Techniques for Transmission Electron Microscopy* (Amsterdam: Elsevier)

[15] Buseck P, Cowley J and Eyring L 1989 *High-Resolution Transmission Electron Microscopy and Associated Techniques* (Oxford: Oxford University Press)

[16] Kumar C S S R 2013 *UV-VIS and Photoluminescence Spectroscopy for Nanomaterials Characterization* (Heidelberg: Springer)

[17] Kumar C S S R 2012 *Raman Spectroscopy for Nanomaterials Characterization* (Heidelberg: Springer)

[18] Pakiari A H and Jamshidi Z 2007 Interaction of amino acids with gold and silver clusters *J. Phys. Chem.* A **111** 4391–6

[19] Barmparis G D, Lodziana Z, Lopez N and Remediakis I N 2015 Nanoparticle shapes by using Wulff constructions and first-principles calculations *Beilstein J. Nanotechnol.* **6** 361–8

[20] Abdalmoneam M H, Waters K, Saikia N and Pandey R 2017 Amino-acid-conjugated gold clusters: interaction of alanine and tryptophan with Au_8 and Au_{20} *J. Phys. Chem.* C **121** 25585–93

[21] Meena S K and Sulpizi M 2013 Understanding the microscopic origin of gold nanoparticle anisotropic growth from molecular dynamics simulations *Langmuir* **29** 14954–61

[22] Meena S K and Sulpizi M 2016 From gold nanoseeds to nanorods: the microscopic origin of the anisotropic growth *Angew. Chem., Int. Ed.* **55** 11960–4

[23] Meena S K, Celiksoy S, Schäfer P, Henkel A, Sönnichsen C and Sulpizi M 2016 The role of halide ions in the anisotropic growth of gold nanoparticles: a microscopic, atomistic perspective *Phys. Chem. Chem. Phys.* **18** 13246–54

[24] Cortes-Huerto R, Goniakowski J and Noguera C 2013 An efficient many-body potential for the interaction of transition and noble metal nano-objects with an environment *J. Chem. Phys.* **138** 244706

[25] Cortes-Huerto R, Goniakowski J and Noguera C 2015 Role of the environment in the stability of anisotropic gold particles *Phys. Chem. Chem. Phys.* **17** 6305–13

[26] Shao Q and Hall C K 2016 Binding preferences of amino acids for gold nanoparticles: a molecular simulation study *Langmuir* **32** 7888–96

[27] Dobrev P, Vemulapalli S P B, Nath N, Griesinger C and Grubmüller H 2020 Probing the accuracy of explicit solvent constant ph molecular dynamics simulations for peptides *J. Chem. Theory Comput.* **16** 2561–9

[28] Klinger M and Jäger A 2015 Crystallographic tool box (CrysTBox): automated tools for transmission electron microscopists and crystallographers *J. Appl. Crystallogr.* **48** 2012–8

[29] Espinoza S and Stepanek J 2010 Raman study of magnesium induced conversion of polyU-polyA duplexes to polyU-polyA-polyU triplexes *J. Spectrosc.* **24** 445–8

[30] Ottova P, Espinoza S and Stepanek J 2011 Magnesium effect on premelting transitions in nucleic acids: DNA duplex and RNA hairpin models *J. Mol. Struct.* **993** 324–7

[31] MacKerell A D *et al* 1998 All-atom empirical potential for molecular modeling and dynamics studies of proteins *J. Phys. Chem.* B **102** 3586–616

[32] Kumar S, Bouzida D, Swendsen R H, Kollman P A and Rosenberg J M 1992 The weighted histogram analysis method for free-energy calculations on biomolecules. I. The method *J. Comput. Chem.* **13** 1011–21

[33] Hess B, Kutzner C, van der Spoel D and Lindahl E 2008 GROMACS 4: algorithms for highly efficient, load-balanced, and scalable molecular simulation *J. Chem. Theory Comput.* **4** 435–47

[34] Pronk S *et al* 2013 GROMACS 4.5: a high-throughput and highly parallel open source molecular simulation toolkit *Bioinformatics* **29** 845–54

[35] Vanommeslaeghe K and MacKerell A D Jr 2012 Automation of the CHARMM general force field (CGenFF) I: bond perception and atom typing *J. Chem. Inf. Model.* **52** 3144–54

[36] Vanommeslaeghe K, Raman E P and MacKerell A D Jr 2012 Automation of the CHARMM general force field (CGenFF) II: assignment of bonded parameters and partial atomic charges *J. Chem. Inf. Model.* **52** 3155–68

[37] Geada I L, Ramezani-Dakhel H, Jamil T, Sulpizi M and Heinz H 2018 Insight into induced charges at metal surfaces and biointerfaces using a polarizable Lennard–Jones potential *Nat. Commun.* **9** 716

[38] Dunlap R A 2018 *Novel Microstructures for Solids* (Bristol: Morgan & Claypool Publishers)

[39] Golichenko B O, Naseka V M, Strelchuk V V and Kolomys O F 2017 Raman study of L-asparagine and L-glutamine molecules adsorbed on aluminum films in a wide frequency range *Semicond. Phys. Quantum Electron. Optoelectron.* **20** 297–304

[40] Moreno A J D, Freire P T C, Melo F E A, Filho J M, Nogueira M A M, Almeida J M A, Miranda M A R, Remédios C M R and Sasaki J M 2004 Low-temperature Raman spectra of monohydrated L-asparagine crystals *J. Raman Spectrosc.* **35** 236–41

[41] Casado J, LÓPez Navarrete J T and Ramírez F J 1995 Infrared and Raman spectra of L-asparagine and L-asparagine-d_5 in the solid state *J. Raman Spectrosc.* **26** 1003–8

[42] Dhamelincourt P and Ramirez F J 1993 Polarized micro-Raman and FT-IR spectra of L-glutamine *Appl. Spectrosc.* **47** 446–51

[43] Barth A 2000 The infrared absorption of amino acid side chains *Prog. Biophys. Mol. Biol.* **74** 141–73

[44] Ramírez F J, Tuñón I and Silla E 1998 Amino acid chemistry in solution: structural study and vibrational dynamics of glutamine in solution. An *ab initio* reaction field model *J. Phys. Chem.* B **102** 6290–8

[45] Wulff G 1901 Z. *Kristallogr.* **34** 449

[46] Mottet C, Tréglia G and Legrand B 1997 New magic numbers in metallic clusters: an unexpected metal dependence *Surf. Sci.* **383** L719–27

[47] Vitos L, Ruban A V, Skriver H L and Kollár J 1998 The surface energy of metals *Surf. Sci.* **411** 186–202

[48] Ascencio J A, Perez M and Jose-Yacaman M 2000 A truncated icosahedral structure observed in gold nanoparticles *Surf. Sci.* **447** 73–80